

Portable Magnetometry for Detection of Biomagnetism in Ambient Environments

M.E. Limes^{1,*}, E.L. Foley,¹ T.W. Kornack,¹ S. Caliga,² S. McBride,² A. Braun,² W. Lee^{1,3},
V.G. Lucivero³, and M.V. Romalis³

¹*Twinleaf LLC, 300 Deer Creek Drive, Plainsboro, New Jersey 08536, USA*

²*SRI International, 201 Washington Road, Princeton, New Jersey 08540, USA*

³*Department of Physics, Princeton University, Princeton, New Jersey 08544, USA*



(Received 7 April 2020; revised 22 June 2020; accepted 1 July 2020; published 20 July 2020)

We present a method of optical magnetometry with parts-per-billion resolution that is able to detect biomagnetic signals generated from the human brain and heart in Earth's ambient environment. Our magnetically silent sensors measure the total magnetic field by detecting the free-precession frequency in a highly spin-polarized alkali-metal vapor. A first-order gradiometer is formed from two magnetometers that are separated by a 3-cm baseline. Our gradiometer operates from a laptop consuming 5 W over a USB port, enabled by state-of-the-art microfabricated alkali-vapor cells, advanced thermal insulation, custom electronics, and compact lasers within the sensor head. The gradiometer has a sensitivity of 16 fT/cm/Hz^{1/2} outdoors, which we use to detect neuronal electrical currents and magnetic cardiography signals. Recording of neuronal magnetic fields is one of a few available methods for noninvasive functional brain imaging that usually requires extensive magnetic shielding and other infrastructure. This work demonstrates the possibility of a dense array of portable biomagnetic sensors that are deployable in a variety of natural environments.

DOI: [10.1103/PhysRevApplied.14.011002](https://doi.org/10.1103/PhysRevApplied.14.011002)

Magnetoencephalography (MEG) and electroencephalography (EEG) serve as important windows into human brain function by providing neuronal-current source imaging with millisecond resolution—much faster than other noninvasive techniques, such as functional magnetic resonance imaging (fMRI), near infrared spectroscopy (NIRS), and positron-emission tomography (PET) [1]. MEG also has several advantages over EEG, including improved source localization and noncontact measurements [2]. Commercially available MEG systems use superconducting quantum interference device (SQUID) magnetometers or gradiometers with a sensitivity of 3–10 fT/Hz^{1/2}. However, existing MEG systems require large expensive magnetically shielded rooms or human-scale magnetic shields, as well as dewars and infrastructure for cryogenic operation. Placing subjects in a magnetically shielded room restricts the range of behaviors and activities that can potentially be studied. There are a few demonstrations of MEG detection using SQUIDS in an unshielded environment [3–5] but such recordings rely on third-order gradiometers that are primarily sensitive to shallow neuronal-current sources. SQUID gradiometers are fundamentally limited in the cancellation of uniform magnetic fields by the fabrication tolerances of their pick-up coils.

As an alternative to the cryogenically cooled and bulky SQUID MEG systems, there has been a recent surge in research into optically pumped magnetometers for MEG detection. Most sensitive atomic magnetometers operate using alkali vapors near zero field in a spin-exchange relaxation-free (SERF) regime [6]. SERF magnetometers have been used for detection [7–13] and localization [14–17] of MEG signals but still require magnetic shielding or field cancellation because their operation relies on having a small total magnetic field. In addition, they require individual calibration and have inherently limited linearity and dynamic range. All measurements with wearable SERF magnetometers have been performed so far in magnetically shielded rooms [16,18].

We present a method of operating a portable optical gradiometric sensor that is able to detect MEG signals in Earth's ambient magnetic field, all while exposed to natural magnetic noise sources. Our technique uses two total-field magnetometers that directly measure the Larmor-precession frequency of alkali-vapor electron spins in the magnetic field. Frequency measurements have a much greater dynamic range and linearity compared to voltage measurements associated with other magnetic field sensors. Furthermore, they do not require individual calibration, so we simply subtract the frequencies recorded from two alkali-vapor cells to find a first-order magnetic field gradient. In principle, a first-order gradiometer allows for

*limes.mark@gmail.com

the detection of deeper current sources. We demonstrate the performance of our sensor by detecting MEG in Earth's ambient environment, as well detecting human heartbeats in real time in magnetically noisy environments. Another recent demonstration of MEG detection with scalar magnetometers [19] requires active magnetic shielding and achieves high sensitivity only at a fraction of Earth's field.

Portable biomagnetic sensor. Our portable gradiometer uses two $8 \times 8 \times 12.5 \text{ mm}^3$ ^{87}Rb vapor cells separated by 3 cm. These cells have anodically bonded glass windows with internal mirrors for 795-nm light [20]. The cells are evacuated, baked, and filled with enriched ^{87}Rb and 650 Torr N_2 . In operation, they are electrically heated inside of radiation shielding with low magnetic noise [21]. The cells are attached to a glass substrate

with low-thermal-conduction supports and placed into an evacuated and sealed $6.5 \times 1.8 \times 1.8 \text{ cm}^3$ cuvette that maintains high vacuum, eliminating gas conduction and convection. This assembly requires 30 mW per cell to heat to the operating temperature of 100°C , giving a ^{87}Rb density of about 5×10^{12} atoms/ cm^3 . The vacuum packaging and low-power laser modules result in an outside surface temperature of 32°C , below body temperature.

As shown in Fig. 1(a), we form a magnetic gradiometer by orienting the two alkali-vapor cells such that multipass laser beams optically pump and probe ^{87}Rb in a plane transverse to Earth's field $B_E \approx 51.4 \mu\text{T}$. The multipass pump is used in favor of a single-pass pump that has previously been used [22] due to geometrical constraints imposed by the radiation shielding. Thus the high-intensity

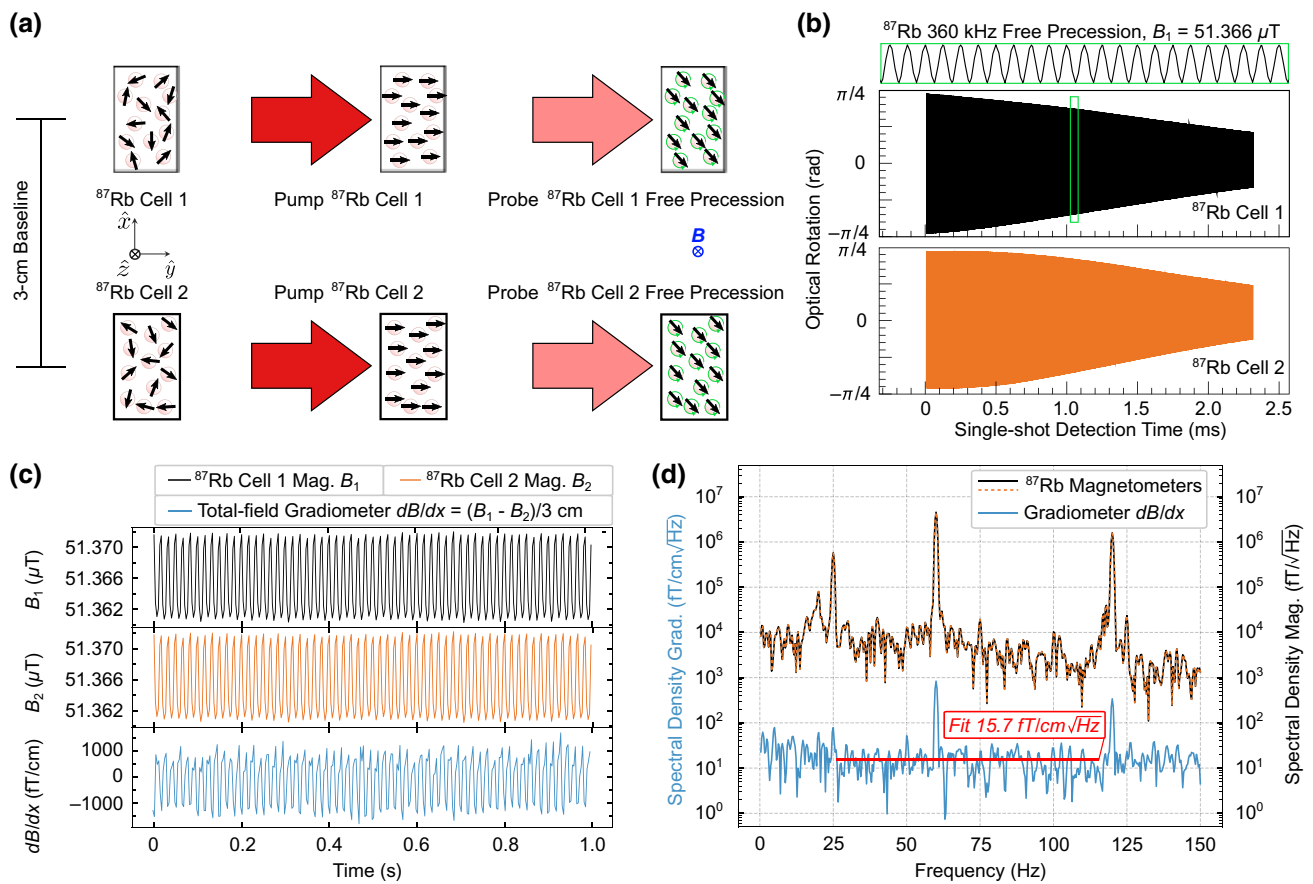


FIG. 1. Magnetic gradiometer operation. (a) Two ^{87}Rb vapor cells separated by a 3-cm baseline are optically pumped with a laser to near-unity polarization. A quantum nondemolition measurement of the ^{87}Rb polarization along the probe axis occurs with a weak detuned laser undergoing optical rotation. ^{87}Rb undergoes free precession about a total field B , leading to a decaying sine-wave signal for each magnetometer cell. The total field B and the quantization axis are determined by the local Earth's field B_E . (b) A custom frequency counter extracts ^{87}Rb free-precession frequencies for each cell by detecting optical-rotation zero crossings in a single-shot detection period of 2.3 ms. The counter calculates a total field for each cell, B_1 and B_2 , by dividing by the ^{87}Rb gyromagnetic ratio $\gamma/2\pi \approx 7 \text{ kHz}/\mu\text{T}$. (c) The single-shot pump and probe measurement is repeated at a rate of 300 Hz. The two magnetometers (mag.) measure total fields B_1 and B_2 , which are streamed to a laptop and subtracted to obtain the first-order total-field gradient dB/dx . (d) We take spectral densities of the total-field magnetometers and gradiometer time-domain data to demonstrate the unshielded noise floor and common-mode rejection of the all-optical gradiometer in Earth's ambient environment. The red line is a fit to the gradiometer noise floor, giving $15.7 \text{ fT}/\text{cm}/\sqrt{\text{Hz}}$.

pump pulses travel along the path of the probe beam, which limits the dead zone to one dead axis. The total fields that each vapor cell experiences, B_1 and B_2 , are dominated by Earth's field B_E and the direction of B_E determines the quantization axis. The ^{87}Rb atoms are spin-polarized by an on-resonant (D1) 795-nm pulsed-pump diode laser that is able to produce several watts for microsecond pulses. The beam is sent through a polarizer and a $\lambda/4$ wave plate to make σ^+ light for optical pumping. We use a style of optical pumping similar to a conventional Bell-Bloom scheme [23,24], obtaining a high initial atomic spin polarization by pumping synchronously with a pump pulse train at the Larmor frequency that is active only during the state initialization period. ^{87}Rb atomic spins are pumped in the transverse plane to near-unity polarization, which causes a suppression of the dominant spin-exchange relaxation mechanism between the $F = 2$ and $F = 1$ hyperfine manifolds at these sizable magnetic fields and leads to an extension in the ^{87}Rb coherence time T_2 [22,25]. We then stop pumping and detect the magnetic field during a ^{87}Rb free-precession period to eliminate frequency shifts associated with the pump laser. A 0.1-mW linearly polarized vertical-cavity surface-emitting laser (VCSEL) probe beam is far detuned from resonance (D1) and undergoes paramagnetic Faraday rotation in a multipass configuration that yields high signal-to-noise [26–28]. The probes of each cell are sent into balanced polarimeters that measure signals corresponding to ^{87}Rb free precession about the total field, as shown in Fig. 1(b). After roughly 1 ms of state initialization and dead time, our acquisition time is 2.3 ms per shot. The entirety of the optics and lasers are housed in a three-dimensionally printed case along with a photodiode-amplifier (PDA) board.

The gradiometer electronics consist of two 6.4×12.7 cm² PCB boards, each powered by 2.5 W from a USB laptop port (or a 5-V battery). One board controls the sensor heating and probe laser, while the other contains a frequency counter and controls the pump-probe sequence. The frequency counter streams two time-stamped frequencies per acquisition period to LabVIEW for real-time analysis and logging. The power consumption of the boards is dominated by the microcontrollers, although lower-power versions are available. We use a shot-to-shot repetition rate of 300 Hz, which is also the data rate of the fields of both magnetometers streamed to the laptop. Subtracting the two measured fields B_1 and B_2 and dividing by the 3-cm baseline, we find the total-field gradient dB/dx . An example of data received by the computer is shown in Fig. 1(c).

To demonstrate the system's potential for biomagnetic measurements, we show the spectral densities of the streamed magnetometer and gradiometer data in Fig. 1(d) with a human subject's head near the sensor, in a natural environment. The largest peaks observed by the sensor are 60- and 120-Hz components coming from power lines roughly 75 m away. Another prominent peak at 25 Hz that

we find comes from a nearby New Jersey Transit–Amtrak Rail line about 750 m away. Considering the 3-cm baseline, the 60-Hz peak suppression of the gradiometer indicates a common-mode rejection ratio of at least 2000. We obtain a similar noise level measured without a subject and note that it is difficult to separate real gradient noise from the intrinsic noise floor of the gradiometer in an unshielded environment without multiple gradiometers. Ignoring the 60-Hz peak, the average gradiometer spectral noise density between 26 and 115 Hz is 15.7 fT/cm $\sqrt{\text{Hz}}$; this implies a magnetometer noise floor of 33.3 fT/ $\sqrt{\text{Hz}}$, which outperforms commercially available scalar atomic sensors operating unshielded in Earth's field. Within magnetic shielding, the total-field gradiometer achieves 10 fT/cm $\sqrt{\text{Hz}}$ with a field of 50 μT applied [29].

Ambient MEG. Operating in a new regime enabled by the first-order gradiometer, we demonstrate detection of MEG signals in Earth's ambient environment, choosing to focus on auditory evoked field responses. Here, 1-kHz audio stimuli of duration 50 ms are generated with a delivery time randomized in a 2.5 ± 1 s window to prevent subject adaptation. These stimuli are delivered by a nonmagnetic pneumatic earphone that is placed into an ear of the subject. The gradiometer is held by a nonmagnetic mount near the audio cortex above the opposing ear, as the subject rests in a wooden chair. The center of each vacuum-packed alkali-vapor cell is about 1.2 cm away from the head of the subject, which is smaller than typical distances for SQUID magnetometers in conventional MEG systems. This measurement stand-off is determined by cell size and the thickness of the radiation shielding and cell cuvette. A synchronization board is used to ensure the precise time stamping of the audio stimuli referenced to the data streamed from the portable gradiometer system, as shown in Fig. 2(a). The gradiometer is oriented such that Earth's field B_E is aligned to optimize the signal for a current dipole expected from auditory evoked responses, with an example of the subject's orientation with respect to the sensor in Fig. 2(b). Auditory evoked field data are recorded for four subjects in several 5–20-min trials, using different sensor positions and orientation.

In Fig. 2(c), we show MEG data that are filtered and averaged over 462 epochs for a subject during a particular trial. For MEG data analysis, we apply a 0.5–50-Hz band-pass filter, along with 25-, 60-, and 120-Hz notch filters, and observe P40m, N100m, and P150m evoked fields (the relatively fast N100m response is consistent with contralateral stimulation for a relatively short interstimulus interval [30,31]). Auditory evoked signals are detected in all four subjects and the sign of the detected dB/dx peaks is consistent with the orientation of the current dipole observed in previous studies of auditory evoked fields [29]. The orientation of the sensor and head with respect to the Earth's field is critical to MEG operation, as total-field magnetometers are only sensitive to the component of the

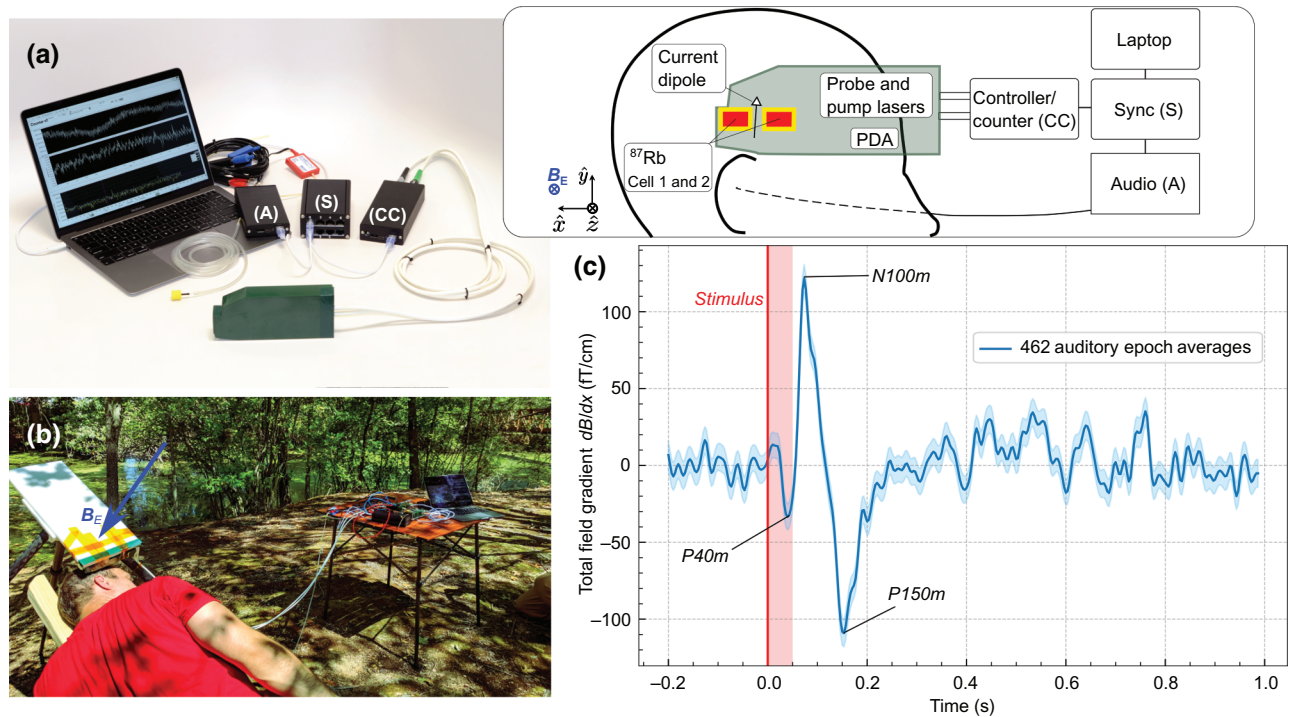


FIG. 2. Auditory evoked fields detected unshielded in Earth's field with a portable first-order gradiometer. (a) The vacuum-packaged ^{87}Rb vapor cells are optically pumped and probed by diode lasers integrated into the gradiometer head. Optical rotation of the probe laser is detected with a photodiode amplifier assembly (PDA). The gradiometer is controlled by compact electronics, including a custom counter that streams the total fields B_1 and B_2 and the gradient dB/dx to the laptop. The two ^{87}Rb vapor cells are placed near a subject's auditory cortex to measure the total-field gradient dB/dx with a 3-cm baseline. The gradiometer is centered approximately over the location of the auditory current dipole, so the radial component of the auditory magnetic field contributes with opposite sign to the two channels. (b) A picture of the in-the-field MEG recording apparatus with a subject. (c) For a given subject, data are recorded for roughly 20 min while time-randomized 1-kHz auditory stimuli are applied to the left ear of the subject. A filtered average of 462 epochs is shown for the dB/dx gradient data taken above a subject's right ear. The bands indicate the standard error of the mean. The auditory evoked fields observed include the prominent N100m peak along with an indication of the P40m and P150m responses.

biomagnetic field parallel to the bias field. Field changes in the transverse plane B_T appear in second-order $B_T^2/2B_E$ and are negligible. Thus when considering arrays of this type of total-field sensor, additional signal processing will be required for making constraints on source localization methods.

We briefly mention another important medical application of sensitive magnetometers, magnetocardiography (MCG). The magnetic fields generated by the heart are stronger but their detection in a magnetically unshielded noisy environment typical of a research laboratory or hospital remains a challenge. A number of optically pumped sensors are being developed for this application [32–35]. In Fig. 3, we show real-time in-the-field MCG signals that are taken by simply walking up and presenting the chest to the sensor, along with a 10-s averaging of human heartbeats. Even in its current form, our sensor is not far from providing a practical MCG device that allows quick electrode-free heart diagnostics for triage in ambient environments.

We present a method of operating optical magnetometers in Earth's natural environment. We show the potential of this technique for biomagnetic measurements through proof-of-principle detections of unshielded MEG and MCG signals using a portable first-order gradiometer. Wearable atomic sensors that do not require shielding will enable a greater variety of MEG research studies, as well as reduce their cost. They can eventually replace EEG sensors currently being used in a variety of open-source EEG systems [36]. By using an all-optical design, we eliminate crosstalk between sensors, which is a deficiency of sensors that require rf or microwave fields. This important feature allows many of these sensors to be formed into a scalable array, which is necessary for proper source localization, as well as to suppress magnetic gradient noise from power lines and other nearby sources, and enables practical operation in a laboratory or hospital environment. We also note that the sensitivity of the gradiometer can be further improved [27] to compete with SQUID sensitivities, while retaining the ability to measure closer to

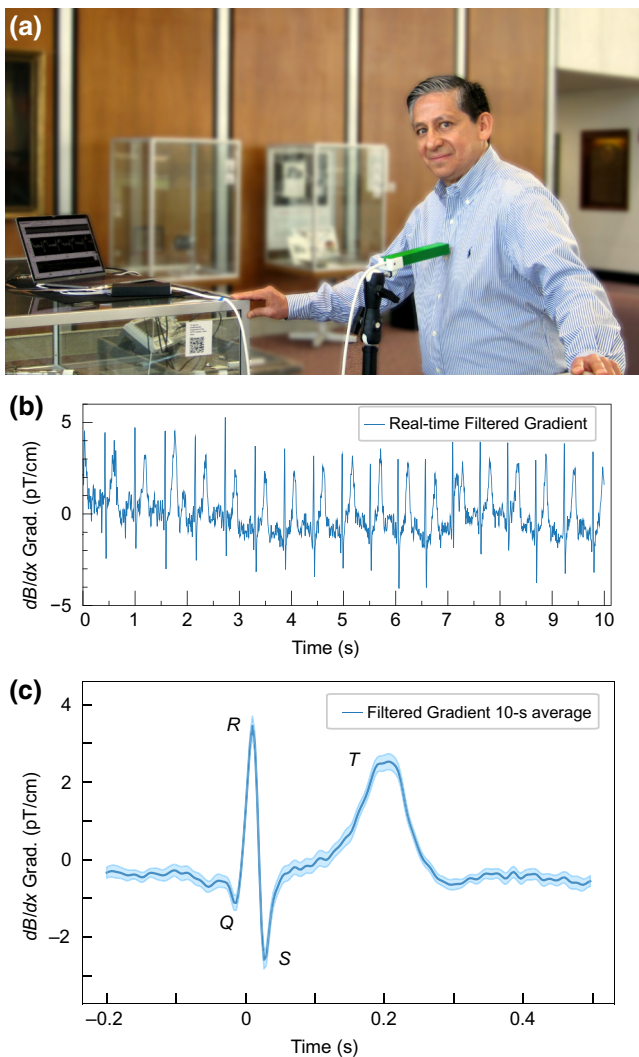


FIG. 3. Field-deployable magnetocardiography. (a) A picture of a next-generation gradiometer that is able to detect human heartbeats in magnetically noisy environments. (b) As the chest of a subject is presented to the sensor, a real-time filter (0.1–50-Hz band-pass, 60- and 120 Hz notches) is applied to the total field gradient dB/dx to demonstrate the heartbeat measurements. (c) The result of averaging data for 10 s, triggered on the *R* peak.

the biomagnetic source than SQUID systems. We believe that the development of these types of portable sensors for ambulatory subjects, which can be used in a cost-effective scalable array, will impact the scope of many MEG and MCG research studies, as well as the host of various other applications that can benefit from a commercially available sensor for total-field magnetometry in Earth's natural environment.

ACKNOWLEDGMENTS

The sensor development was funded by the Defense Advanced Research Projects Agency (DARPA) Microsystems Technology Office (MTO) under Contract No.

140D6318C0020. The views, opinions, and/or findings expressed are those of the authors and should not be interpreted as representing the official views or policies of the Department of Defense or the U.S. Government. Approved for Public Release, Distribution Unlimited. The proof-of-principle demonstrations of the sensor detecting biomagnetic signals were supported by Princeton University and the Fetzer Franklin Fund of the John E. Fetzer Memorial Trust.

- [1] M. Hämäläinen, R. Hari, R. J. Ilmoniemi, J. Knuutila, and O. V. Lounasmaa, Magnetoencephalography—theory, instrumentation, and applications to noninvasive studies of the working human brain, *Rev. Mod. Phys.* **65**, 413 (1993).
- [2] S. Baillet, Magnetoencephalography for brain electrophysiology and imaging, *Nat. Neurosci.* **20**, 327 EP (2017), [Review Article](#).
- [3] J. Vrba, B. Taylor, T. Cheung, A. A. Fife, G. Haid, P. R. Kubik, S. Lee, J. McCubbin, and M. B. Burbank, Noise cancellation by a whole-cortex SQUID MEG system, *IEEE Trans. Appl. Supercond.* **5**, 2118 (1995).
- [4] Y. Okada, K. Pratt, C. Atwood, A. Mascarenas, R. Reineinan, J. Nurminen, and D. Paulson, BabySQUID: A mobile, high-resolution multichannel magnetoencephalography system for neonatal brain assessment, *Rev. Sci. Instrum.* **77**, 024301 (2006).
- [5] Y. Seki, A. Kandori, K. Ogata, T. Miyashita, Y. Kumagai, M. Ohnuma, K. Konaka, and H. Naritomi, Note: Unshielded bilateral magnetoencephalography system using two-dimensional gradiometers, *Rev. Sci. Instrum.* **81**, 096103 (2010).
- [6] I. K. Kominis, T. W. Kornack, J. C. Allred, and M. V. Romalis, A subfemtotesla multichannel atomic magnetometer, *Nature* **422**, 596 (2003).
- [7] H. Xia, A. Ben-Amar Baranga, D. Hoffman, and M. V. Romalis, Magnetoencephalography with an atomic magnetometer, *Appl. Phys. Lett.* **89**, 211104 (2006).
- [8] C. Johnson, P. D. D. Schwindt, and M. Weisend, Magnetoencephalography with a two-color pump-probe, fiber-coupled atomic magnetometer, *Appl. Phys. Lett.* **97**, 243703 (2010).
- [9] T. H. Sander, J. Preusser, R. Mhaskar, J. Kitching, L. Trahms, and S. Knappe, Magnetoencephalography with a chip-scale atomic magnetometer, *Biomed. Opt. Express* **3**, 981 (2012).
- [10] C. N. Johnson, P. D. D. Schwindt, and M. Weisend, Multi-sensor magnetoencephalography with atomic magnetometers, *Phys. Med. Biol.* **58**, 6065 (2013).
- [11] V. K. Shah and R. T. Wakai, A compact, high performance atomic magnetometer for biomedical applications, *Phys. Med. Biol.* **58**, 8153 (2013).
- [12] O. Alem, A. M. Benison, D. S. Barth, J. Kitching, and S. Knappe, Magnetoencephalography of epilepsy with a microfabricated atomic magnetode, *J. Neurosci.* **34**, 14324 (2014).
- [13] J. Sheng, S. Wan, Y. Sun, R. Dou, Y. Guo, K. Wei, K. He, J. Qin, and J.-H. Gao, Magnetoencephalography with

- a Cs-based high-sensitivity compact atomic magnetometer, *Rev. Sci. Instrum.* **88**, 094304 (2017).
- [14] K. Kim, S. Begus, H. Xia, S.-K. Lee, V. Jazbinsek, Z. Trontelj, and M. V. Romalis, Multi-channel atomic magnetometer for magnetoencephalography: A configuration study, *NeuroImage* **89**, 143 (2014).
- [15] E. Boto, S. S. Meyer, V. Shah, O. Alem, S. Knappe, P. Kruger, T. M. Fromhold, M. Lim, P. M. Glover, P. G. Morris, R. Bowtell, G. R. Barnes, and M. J. Brookes, A new generation of magnetoencephalography: Room temperature measurements using optically-pumped magnetometers, *NeuroImage* **149**, 404 (2017).
- [16] E. Boto, N. Holmes, J. Leggett, G. Roberts, V. Shah, S. S. Meyer, L. D. Muñoz, K. J. Mullinger, T. M. Tierney, S. Bestmann, G. R. Barnes, R. Bowtell, and M. J. Brookes, Moving magnetoencephalography towards real-world applications with a wearable system, *Nature* **555**, 657 EP (2018).
- [17] A. Borna, T. R. Carter, A. P. Colombo, Y.-Y. Jau, J. McKay, M. Weisend, S. Taulu, J. M. Stephen, and P. D. D. Schwandt, Non-invasive functional-brain-imaging with an OPM-based magnetoencephalography system, *PLoS ONE* **15**, 1 (2020).
- [18] R. M. Hill, E. Boto, N. Holmes, C. Hartley, Z. A. Seedat, J. Leggett, G. Roberts, V. Shah, T. M. Tierney, M. W. Woolrich, C. J. Stagg, G. R. Barnes, R. R. Bowtell, R. Slater, and M. J. Brookes, A tool for functional brain imaging with lifespan compliance, *Nat. Commun.* **10**, 4785 (2019).
- [19] R. Zhang, W. Xiao, Y. Ding, Y. Feng, X. Peng, L. Shen, C. Sun, T. Wu, Y. Wu, Y. Yang *et al.*, Recording brain activities in unshielded Earth's field with optically pumped atomic magnetometers, *Sci. Adv.* **6**, eaba8792 (2020).
- [20] N. Dural and M. V. Romalis, Anodically bonded cells with optical elements, U.S. Patent 10345548 (2017).
- [21] H. B. Dang, A. C. Maloof, and M. V. Romalis, Ultrahigh sensitivity magnetic field and magnetization measurements with an atomic magnetometer, *Appl. Phys. Lett.* **97**, 151110 (2010).
- [22] V. G. Lucivero, W. Lee, M. V. Romalis, M. E. Limes, E. L. Foley, and T. Kornack, A femtotesla quantum-noise-limited pulsed gradiometer at Earth's magnetic fields (2019), APS DAMOP, <https://meetings.aps.org/Meeting/DAMOP19/Session/E01.37>
- [23] W. E. Bell and A. L. Bloom, Optically Driven Spin Precession, *Phys. Rev. Lett.* **6**, 280 (1961).
- [24] V. Gerginov, S. Krzyzewski, and S. Knappe, Pulsed operation of a miniature scalar optically pumped magnetometer, *J. Opt. Soc. Am. B* **34**, 1429 (2017).
- [25] M. V. Romalis, H. Dong, and A. Baranga, Pulsed scalar atomic magnetometer, U.S. 20180356476a, <https://patents.google.com/patent/US20180356476A1/en> (2018).
- [26] S. Li, P. Vachaspati, D. Sheng, N. Dural, and M. V. Romalis, Optical rotation in excess of 100 rad generated by Rb vapor in a multipass cell, *Phys. Rev. A* **84**, 061403 (2011).
- [27] D. Sheng, S. Li, N. Dural, and M. V. Romalis, Sub-femtotesla Scalar Atomic Magnetometry Using Multipass Cells, *Phys. Rev. Lett.* **110**, 160802 (2013).
- [28] W. Lee, V. G. Lucivero, M. V. Romalis, M. E. Limes, E. L. Foley, and T. Kornack, Heading error analysis of a pulsed ^{87}Rb magnetometer at geomagnetic fields (2019), APS DAMOP, <http://meetings.aps.org/Meeting/DAMOP19/Session/S01.36>
- [29] See the Supplemental Material at <http://link.aps.org/supplemental/10.1103/PhysRevApplied.14.011002> for additional information and figures.
- [30] J. P. Mäkelä, A. Ahonen, M. Hämäläinen, R. Hari, R. Ilmoniemi, M. Kajola, J. Knuutila, O. V. Lounasmaa, L. McEvoy, R. Salmelin, O. Salonen, M. Sams, J. Simola, C. Tesche, and J.-P. Vasama, Functional differences between auditory cortices of the two hemispheres revealed by whole-head neuromagnetic recordings, *Hum. Brain Mapp.* **1**, 48 (1993).
- [31] A. Gutschalk, in *Magnetoencephalography: From Signals to Dynamic Cortical Networks*, edited by S. Supek and C. J. Aine (Springer International Publishing, Cham, 2019), p. 907.
- [32] G. Bison, R. Wynands, and A. Weis, Dynamical mapping of the human cardiomagnetic field with a room-temperature, laser-optical sensor, *Opt. Express* **11**, 904 (2003).
- [33] R. Wyllie, M. Kauer, R. T. Wakai, and T. G. Walker, Optical magnetometer array for fetal magnetocardiography, *Opt. Lett.* **37**, 2247 (2012).
- [34] O. Alem, T. H. Sander, R. Mhaskar, J. LeBlanc, H. Eswaran, U. Steinhoff, Y. Okada, J. Kitching, L. Trahms, and S. Knappe, Fetal magnetocardiography measurements with an array of microfabricated optically pumped magnetometers, *Phys. Med. Biol.* **60**, 4797 (2015).
- [35] M. Bai, Y. Huang, G. Zhang, W. Zheng, Q. Lin, and Z. Hu, Fast backward singular value decomposition (SVD) algorithm for magnetocardiographic signal reconstruction from pulsed atomic magnetometer data, *Opt. Express* **27**, 29534 (2019).
- [36] OpenBCI, <https://openbci.com/>.

SUPPLEMENTARY INFORMATION

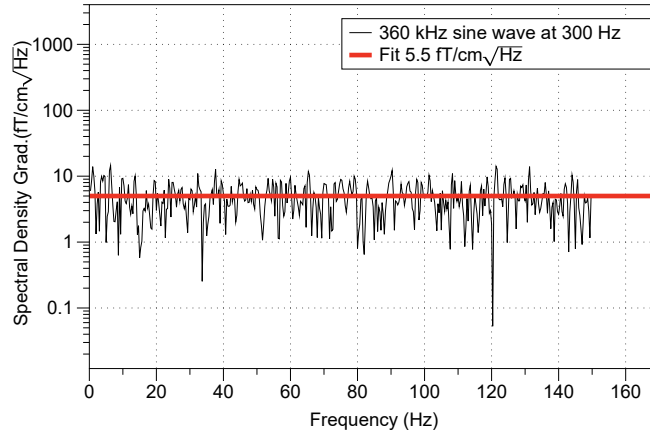


FIG. 1. The custom frequency counter is set up under the operating conditions used in the main text, triggered on 300 Hz and acquisition window of 2.3 ms. 360 kHz sine waves from a function generator are sent into the two channels. A fit to the white noise gives our reported portable detection noise floor of $5.5 \text{ fT/cm}\sqrt{\text{Hz}}$.

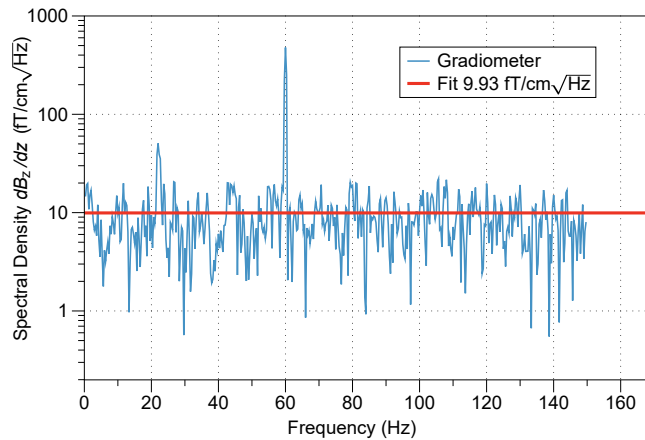


FIG. 2. Spectral density of gradiometer in magnetic shielding (Twinleaf MS-2), taken with $49.3 \mu\text{T}$ bias field.

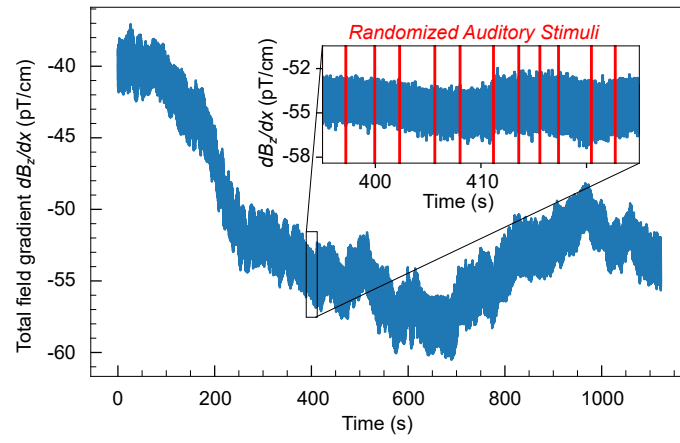


FIG. 3. The raw dB_z/dx gradient data shown averaged in Fig. 3 of the main text.

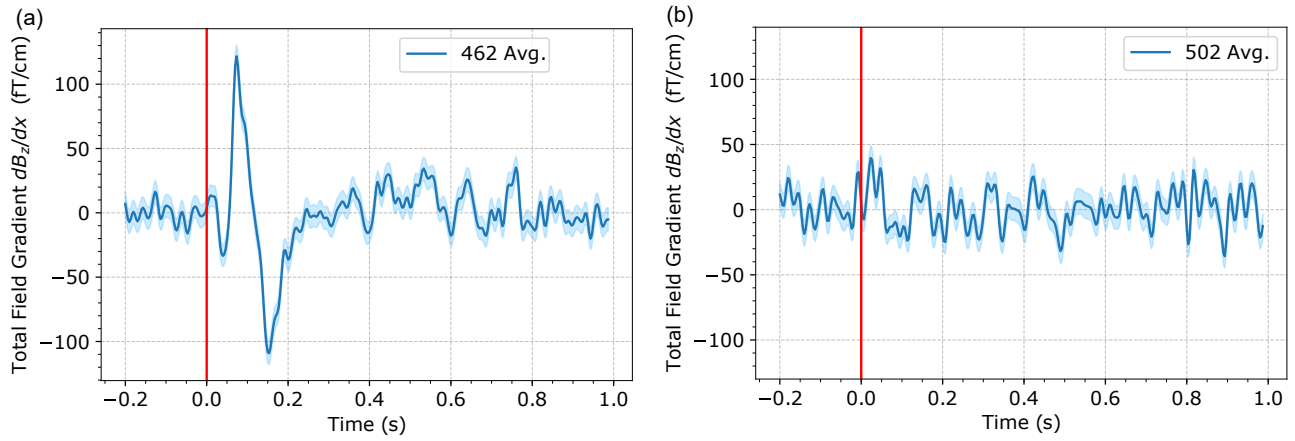


FIG. 4. Data for subject with (a) and without (b) auditory stimuli.

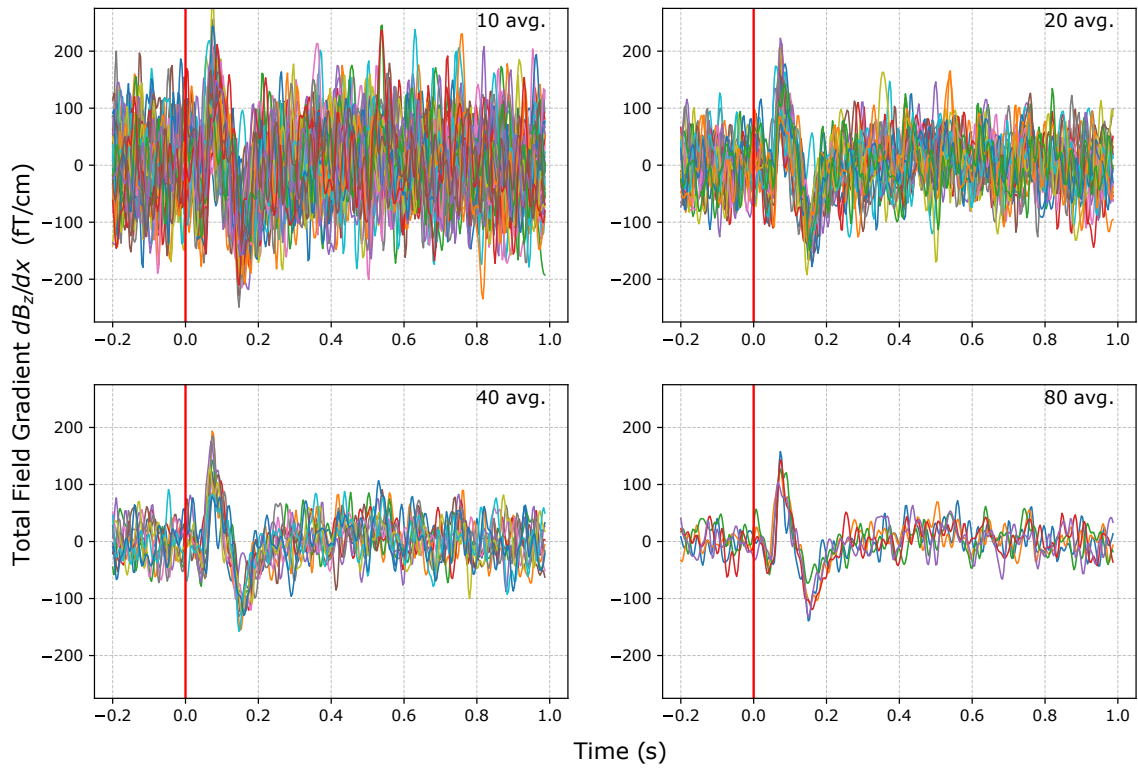


FIG. 5. Taking averages (10, 20, 40, and 80) of the data taken shown in Fig. 3 of the main text.

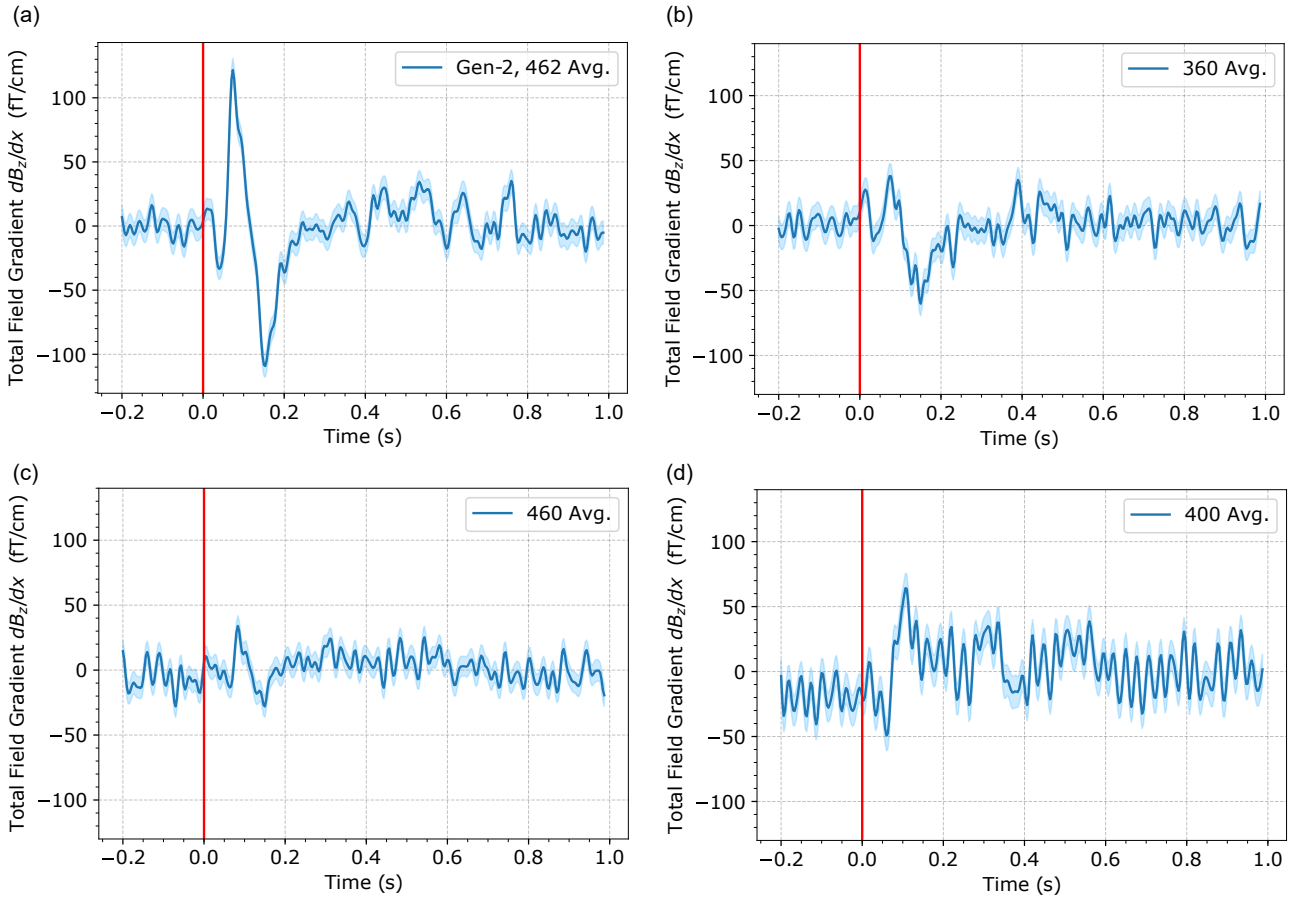


FIG. 6. Data taken for four different subjects showing auditory evoked fields. Note the orientation of the sensor relative to the subject's head was opposite for subject (d). The positioning of the sensor was done by eye, which explains the variability of the signal size along with natural MEG signal variability among subjects.